Atmospheric effects on spatial frequency bounds on polarimeter imaging[1]

Maj David M. Strong
PhD Student
Department of Electrical and Computer Engineering
Graduate School of Engineering and Management
2950 Hobson Way
Air Force Institute of Technology
Wright-Patterson AFB, OH 45433

Abstract

The intent of this paper is to extend a previously developed [2] statistical model of a polarimetric sensor to include atmospheric effects on the spatial frequency bound. Initial estimates of the spatial frequency resolution are attained through calculation of the Cramer-Rao lower bound for a two-channel polarimeter in a vacuum. The definition of maximum spatial frequency resolution for this research is when the highest spatial frequencies observed just meet the noise floor. Previous results for the model in a vacuum showed that the spatial resolution bound is lowered as the degree of polarization in the image is varied from 0 to 1. Before pursuing a blind deconvolution algorithm for a polarimeter it is important to understand the impact of atmospheric effects on the spatial frequency bound. The model used for the polarimeter imaging system is an ideal two-channel polarimeter with an output of two images of orthogonal polarizations. Models of the atmosphere with various amounts of turbulence are then added to the polarimeter imaging system model to determine the impact on the spatial frequency bound. The number of Zernike coefficients used to model the atmospheric distortions and their impact on the spatial frequency bound is also explored. Additionally, the impact on the bound through the use of a simulated adaptive optic system to reduce the atmospheric turbulence effect on the polarimeter images is shown. The data produced by the developed models is then used to determine the potential for developing new algorithms to improve existing polarimeter imaging capabilities.

1 Introduction

This paper continues the development of the Cramer-Rao lower bounds (CRLB) and analysis of the bounds for an idealized two-channel polarimeter. The first section, Section 2, extends both the normal imaging system case and the two channel polarimeter case to include the effects of atmospheric distortion. The second section, Section 3, discusses the results of the CRLBs as various parameters are changed. The final section, Section 4, concludes with an analysis of the performance differences between a normal imaging system and a two-channel polarimeter.

Similar to the previous development, two point sources comprise the image modeled. The parameters in the model are expanded to include the individual Zernike coefficients. The scenario still assumes a perfect polarizing beam splitter (PBS) to produce the two images with no light lost. The parameters estimated are the amplitudes of the two point sources (o_{0h},o_{0v},o_{1h} and o_{1v}), the separation distance (Δ), and a set of Zernike parameters (a_2,a_3,...,a_{n-1},a_n). For analytical purposes this requires a separate Fisher Information (FI) matrix for every set of Zernike coefficients estimated. Once the FI matrix is developed, its individual elements are populated and then it is inverted. The CRLBs for the individual parameters estimated are located along the diagonal of the inverted FI matrix. The average CRLBs are then produced from the averaging of multiple instantiations of the FI matrix. Each instantiation of the FI matrix is created by

[1]The views expressed in this article are those of the author and do not reflect the official policy of the United States Air Force, Department of Defense, or the United States Government.

randomly generated Zernike coefficients. The coefficients are generated within the statistical bounds of a predetermined covariance matrix representative of atmospheric turbulence.

2 Development of the CRLB

The development of the CRLB for an imaging system, whether it's a normal system or a polarimeter, requires several things. First it requires a statistical model of the images produced and is represented by its probability mass function (*PMF*). Next the log-likelihood function is produced by taking the log of the PMF. The partial derivatives of the log-likelihood function along with the image itself are used to populate the FI matrix. Finally the FI matrix is populated and its inverse is calculated to produce the individual CRLBs along its diagonal.

2.1 Image Model

The derivation of the CRLBs starts with an image model. The same probability is used for development of the CRLB for a scenario using a sensor that captures two simultaneous images using the two different polarity channels produced by a PBS:

$$PMF = \prod_x \prod_y \left(\frac{i_h(x,y;\alpha)^{d_h(x,y)} exp^{-i_h(x,y;\alpha)}}{d_h(x,y)!}\right) \cdot \left(\frac{i_v(x,y;\alpha)^{d_v(x,y)} exp^{-i_v(x,y;\alpha)}}{d_v(x,y)!}\right) \tag{1}$$

The image definitions for notation purposes arbitrarily define one image as the horizontally (h) polarized image and the other as the vertically (v) polarized image. The individual images are thus defined, similarly to the base case, as

$$\begin{aligned} i(x,y;\alpha) &= i_h(x,y;\alpha) + i_v(x,y;\alpha) & (2)\\ &= \sum_z \sum_w h(x-z, y-w;\alpha)((o_{0h}+o_{0v})\delta(z,w) + (o_{1h}+o_{1v})\delta(z-\Delta,w)) & (3) \end{aligned}$$

where $h(x,y;\alpha)$ is the point spread function (*psf*).

2.1.1 The Point Spread Function

To account for atmospheric turbulence and the effect of the imaging system in closer approximation to reality, a more accurate model of the *psf* than previously developed is required. With the assumption of an abberation free imaging system and a point source sufficiently far away that its field arrives at the aperture as a plane wave. Therefore, its image is the Fourier transform of the field masked by the pupil function multiplied by the wave abberation function caused by the atmosphere. This yields the *psf*

$$\begin{aligned} h(x,y;\alpha) &= \left| \mathscr{F}\left\{ P(f_x,f_y) exp\left[j \sum_n a_n \phi_n(f_x,f_y) \right] \right\} \right|^2 & (4)\\ &= \left| \int\int P(f_x,f_y) exp\left[j \sum_n a_n \phi_n(f_x,f_y) \right] exp\left[-j2\pi(f_x x + f_y y)\right] df_x df_y \right|^2 & (5) \end{aligned}$$

and the *psf* for the shifted point is

$$\begin{aligned} h(x-\Delta,y;\alpha) &= \left| \int\int P(f_x,f_y) exp\left[j \sum_n a_n \phi_n(f_x,f_y) \right] exp\left[-j2\pi(f_x(x-\Delta) + f_y y)\right] df_x df_y \right|^2 & (6)\\ &= \left| \int\int P(f_x,f_y) exp\left[j \sum_n a_n \phi_n(f_x,f_y) \right] exp\left[-j2\pi(f_x x + f_y y)\right] exp[j2\pi f_x \Delta] df_x df_y \right|^2 & (7) \end{aligned}$$

Thus $h(x-\Delta,y;\alpha)$ is equal to $h(x,y;\alpha)$ shifted by Δ using the Fourier transform shift theorem.

2.2 Log-likelihood Function

The log-likelihood function for the dual polarity case is found by taking the log of the PMF as shown in Eqn. 1. It is a function of all the parameters estimated in the model.

$$L(\Delta, o_{0h}, o_{0v}, o_{1h}, o_{1v}, a_2, a_3, ..., a_{n-1}, a_n) = ln(PMF) \tag{8}$$

$$\approx \sum_x \sum_y [d_h(x,y) ln(i_h(x,y;\alpha)) - i_h(x,y;\alpha) + d_v(x,y) ln(i_v(x,y;\alpha)) - i_v(x,y;\alpha)] \tag{9}$$

2.3 Polarimeter Fisher Information Matrix

The Fisher information matrix is composed of the expected values of the partial derivatives of the log-likelihood function[3]. The individual elements in the FI matrix are

$$J_{ij} = E\left[-E\left[\frac{\delta^2 L(\Delta, o_{0h}, o_{0v}, o_{1h}, o_{1v}, a_2, a_3, ..., a_{n-1}, a_n)}{\delta_{L_i} \delta_{L_j}}\right] |\alpha\right] \tag{10}$$

$$= E\left[\sum_x \sum_y \left[\frac{1}{i_h(x,y;\alpha)} \frac{\delta i_h(x,y;\alpha)}{\delta L_i} \frac{\delta i_h(x,y;\alpha)}{\delta L_j} + \frac{1}{i_v(x,y;\alpha)} \frac{\delta i_v(x,y;\alpha)}{\delta L_i} \frac{\delta i_v(x,y;\alpha)}{\delta L_j}\right]\right] \tag{11}$$

such that

$$J = \begin{bmatrix} J_{\Delta\Delta} & J_{\Delta o_{0h}} & J_{\Delta o_{0v}} & J_{\Delta o_{1h}} & J_{\Delta o_{1v}} & J_{\Delta a_1} & J_{\Delta a_2} & & J_{\Delta a_{n-1}} & J_{\Delta a_n} \\ J_{o_{0h}\Delta} & J_{o_{0h}o_{0h}} & J_{o_{0h}o_{0v}} & J_{o_{0h}o_{1h}} & J_{o_{0h}o_{1v}} & J_{o_{0h}a_1} & J_{o_{0h}a_2} & & J_{o_{0h}a_{n-1}} & J_{o_{0h}a_n} \\ J_{o_{0v}\Delta} & J_{o_{0v}o_{0h}} & J_{o_{0v}o_{0v}} & J_{o_{0v}o_{1h}} & J_{o_{0v}o_{1v}} & J_{o_{0v}a_1} & J_{o_{0v}a_2} & \cdots & J_{o_{0v}a_{n-1}} & J_{o_{0v}a_n} \\ J_{o_{1h}\Delta} & J_{o_{1h}o_{0h}} & J_{o_{1h}o_{0v}} & J_{o_{1h}o_{1h}} & J_{o_{1h}o_{1v}} & J_{o_{1h}a_1} & J_{o_{1h}a_2} & & J_{o_{1h}a_{n-1}} & J_{o_{1h}a_n} \\ J_{o_{1v}\Delta} & J_{o_{1v}o_{0h}} & J_{o_{1v}o_{0v}} & J_{o_{1v}o_{1h}} & J_{o_{1v}o_{1v}} & J_{o_{1v}a_1} & J_{o_{1v}a_2} & & J_{o_{1v}a_{n-1}} & J_{o_{1v}a_n} \\ J_{a_1\Delta} & J_{a_1o_{0h}} & J_{a_1o_{0v}} & J_{a_1o_{1h}} & J_{a_1o_{1v}} & J_{a_1a_1} & J_{a_1a_2} & & J_{a_1a_{n-1}} & J_{a_1a_n} \\ J_{a_2\Delta} & J_{a_2o_{0h}} & J_{a_2o_{0v}} & J_{a_2o_{1h}} & J_{a_2o_{1v}} & J_{a_2a_1} & J_{a_2a_2} & & J_{a_2a_{n-1}} & J_{a_2a_n} \\ & & \vdots & & & & & \ddots & & \\ J_{a_{n-1}\Delta} & J_{a_{n-1}o_{0h}} & J_{a_{n-1}o_{0v}} & J_{a_{n-1}o_{1h}} & J_{a_{n-1}o_{1v}} & J_{a_{n-1}a_1} & J_{a_{n-1}a_2} & & J_{a_{n-1}a_{n-1}} & J_{a_{n-1}a_n} \\ J_{a_n\Delta} & J_{a_no_{0h}} & J_{a_no_{0v}} & J_{a_no_{1h}} & J_{a_no_{1v}} & J_{a_na_1} & J_{a_na_2} & & J_{a_na_{n-1}} & J_{a_na_n} \end{bmatrix} \tag{12}$$

However, since the cross Zernike terms result in zeros the Fisher information matrix simplifies to

$$J = \begin{bmatrix} J_{\Delta\Delta} & J_{\Delta o_{0h}} & J_{\Delta o_{0v}} & J_{\Delta o_{1h}} & J_{\Delta o_{1v}} & J_{\Delta a_1} & J_{\Delta a_2} & & J_{\Delta a_{n-1}} & J_{\Delta a_n} \\ J_{o_{0h}\Delta} & J_{o_{0h}o_{0h}} & J_{o_{0h}o_{0v}} & J_{o_{0h}o_{1h}} & J_{o_{0h}o_{1v}} & J_{o_{0h}a_1} & J_{o_{0h}a_2} & & J_{o_{0h}a_{n-1}} & J_{o_{0h}a_n} \\ J_{o_{0v}\Delta} & J_{o_{0v}o_{0h}} & J_{o_{0v}o_{0v}} & J_{o_{0v}o_{1h}} & J_{o_{0v}o_{1v}} & J_{o_{0v}a_1} & J_{o_{0v}a_2} & \cdots & J_{o_{0v}a_{n-1}} & J_{o_{0v}a_n} \\ J_{o_{1h}\Delta} & J_{o_{1h}o_{0h}} & J_{o_{1h}o_{0v}} & J_{o_{1h}o_{1h}} & J_{o_{1h}o_{1v}} & J_{o_{1h}a_1} & J_{o_{1h}a_2} & & J_{o_{1h}a_{n-1}} & J_{o_{1h}a_n} \\ J_{o_{1v}\Delta} & J_{o_{1v}o_{0h}} & J_{o_{1v}o_{0v}} & J_{o_{1v}o_{1h}} & J_{o_{1v}o_{1v}} & J_{o_{1v}a_1} & J_{o_{1v}a_2} & & J_{o_{1v}a_{n-1}} & J_{o_{1v}a_n} \\ J_{a_1\Delta} & J_{a_1o_{0h}} & J_{a_1o_{0v}} & J_{a_1o_{1h}} & J_{a_1o_{1v}} & J_{a_1a_1} & 0 & & 0 & 0 \\ J_{a_2\Delta} & J_{a_2o_{0h}} & J_{a_2o_{0v}} & J_{a_2o_{1h}} & J_{a_2o_{1v}} & 0 & J_{a_2a_2} & & 0 & 0 \\ & & \vdots & & & & & \ddots & & \\ J_{a_{n-1}\Delta} & J_{a_{n-1}o_{0h}} & J_{a_{n-1}o_{0v}} & J_{a_{n-1}o_{1h}} & J_{a_{n-1}o_{1v}} & 0 & 0 & & J_{a_{n-1}a_{n-1}} & 0 \\ J_{a_n\Delta} & J_{a_no_{0h}} & J_{a_no_{0v}} & J_{a_no_{1h}} & J_{a_no_{1v}} & 0 & 0 & & 0 & J_{a_na_n} \end{bmatrix} \tag{13}$$

2.4 Polarimeter Image Derivatives

The individual partial derivatives of the image with respect to each of the parameters estimated are

$$\frac{\partial i_n(x,y;\alpha)}{\partial \Delta} = o_{1n} \frac{\partial}{\partial \Delta} h(x-\Delta, y; \alpha) \tag{14}$$

$$\frac{\partial i_h(x,y;\alpha)}{\partial o_{0h}} = h(x,y;\alpha) \tag{15}$$

$$\frac{\partial i_h(x,y;\alpha)}{\partial o_{0v}} = 0 \tag{16}$$

$$\frac{\partial i_h(x,y;\alpha)}{\partial o_{1h}} = h(x-\Delta, y; \alpha) \tag{17}$$

$$\frac{\partial i_h(x,y;\alpha)}{\partial o_{1v}} = 0 \tag{18}$$

$$\frac{\partial i_v(x,y;\alpha)}{\partial o_{0h}} = 0 \tag{19}$$

$$\frac{\partial i_v(x,y;\alpha)}{\partial o_{0v}} = h(x,y;\alpha) \tag{20}$$

$$\frac{\partial i_v(x,y;\alpha)}{\partial o_{1h}} = 0 \tag{21}$$

$$\frac{\partial i_v(x,y;\alpha)}{\partial o_{1v}} = h(x-\Delta, y; \alpha) \tag{22}$$

$$\frac{\partial i_h(x,y;\alpha)}{\partial a_n} = o_{0h}\frac{\partial}{\partial a_n}h(x,y;\alpha) + o_{1h}\frac{\partial}{\partial a_n}h(x-\Delta,y;\alpha) \quad (23)$$

$$\frac{\partial i_v(x,y;\alpha)}{\partial a_n} = o_{0v}\frac{\partial}{\partial a_n}h(x,y;\alpha) + o_{1v}\frac{\partial}{\partial a_n}h(x-\Delta,y;\alpha) \quad (24)$$

These partial derivatives are then used in combinations to populate the FI matrix. However, they still require partial derivatives of the *psf* to be written in an explicit form. Using the identity $|f|^2 = f \cdot f^*$ and letting $f_2 = f_1^*$, the *psf* is decomposed into $h(x,y;\alpha) = f_1 \cdot f_2$ where

$$f_1 = \int\int P(f_x,f_y) exp\left[j\sum_n a_n\phi_n(f_x,f_y)\right] exp\left[-j2\pi(f_x x + f_y y)\right] df_x df_y. \quad (25)$$

The partial derivative of the *psf* with respect to Δ is therefore

$$\frac{\partial}{\partial\Delta}h(x-\Delta,y;\alpha) = \frac{\partial}{\partial\Delta}\left[f_1 \cdot f_2\right]. \quad (26)$$

Using the chain rule this becomes

$$f_1 \cdot \left[\frac{\partial}{\partial\Delta}f_2\right] + \left[\frac{\partial}{\partial\Delta}f_1\right] \cdot f_2. \quad (27)$$

where

$$\frac{\partial}{\partial\Delta}f_1 = j\int\int (2\pi f_x) P(f_x,f_y) exp\left[j\sum_n a_n\phi_n(f_x,f_y)\right] exp\left[-j2\pi(f_x(x-\Delta) + f_y y)\right] df_x df_y \quad (28)$$

and

$$\frac{\partial}{\partial\Delta}f_2 = \left[\frac{\partial}{\partial\Delta}f_1\right]^* \quad (29)$$

The partial derivatives of the *psf* with respect to the individual Zernike coefficients are similarly

$$\frac{\partial}{\partial a_n}h(x,y;\alpha) = \frac{\partial}{\partial a_n}\left[f_1 \cdot f_2\right] \quad (30)$$

$$= f_1 \cdot \left[\frac{\partial}{\partial a_n}f_2\right] + \left[\frac{\partial}{\partial a_n}f_1\right] \cdot f_2 \quad (31)$$

where

$$\frac{\partial}{\partial a_n}f_1 = j\int\int P(f_x,f_y)\phi_n(f_x,f_y) exp\left[j\sum_n a_n\phi_n(f_x,f_y)\right] exp\left[-j2\pi(f_x x + f_y y)\right] df_x df_y \quad (32)$$

and

$$\frac{\partial}{\partial a_n}f_2 = \left[\frac{\partial}{\partial a_n}f_1\right]^* \quad (33)$$

The partial derivatives of $h(x-\Delta,y;\alpha)$ become $h(x,y;\alpha)$ shifted by Δ.

2.5 CRLB

Using the previous partial derivatives, the FI matrix is filled in and the inverse is calculated. The resulting diagonal elements are the CRLBs for the parameters estimated.

$$\frac{1}{J} = \begin{bmatrix}
\sigma^2_{\epsilon_\Delta} & J^{\Delta o_{0h}} & J^{\Delta o_{0v}} & J^{\Delta o_{1h}} & J^{\Delta o_{1v}} & J^{\Delta a_1} & J^{\Delta a_2} & & J^{\Delta a_{n-1}} & J^{\Delta a_n} \\
J^{o_{0h}\Delta} & \sigma^2_{\epsilon_{o_{0h}}} & J^{o_{0h}o_{0v}} & J^{o_{0h}o_{1h}} & J^{o_{0h}o_{1v}} & J^{o_{0h}a_1} & J^{o_{0h}a_2} & & J^{o_{0h}a_{n-1}} & J^{o_{0h}a_n} \\
J^{o_{0v}\Delta} & J^{o_{0v}o_{0h}} & \sigma^2_{\epsilon_{o_{0v}}} & J^{o_{0v}o_{1h}} & J^{o_{0v}o_{1v}} & J^{o_{0v}a_1} & J^{o_{0v}a_2} & \cdots & J^{o_{0v}a_{n-1}} & J^{o_{0v}a_n} \\
J^{o_{1h}\Delta} & J^{o_{1h}o_{0h}} & J^{o_{1h}o_{0v}} & \sigma^2_{\epsilon_{o_{1h}}} & J^{o_{1h}o_{1v}} & J^{o_{1h}a_1} & J^{o_{1h}a_2} & & J^{o_{1h}a_{n-1}} & J^{o_{1h}a_n} \\
J^{o_{1v}\Delta} & J^{o_{1v}o_{0h}} & J^{o_{1v}o_{0v}} & J^{o_{1v}o_{1h}} & \sigma^2_{\epsilon_{o_{1v}}} & J^{o_{1v}a_1} & J^{o_{1v}a_2} & & J^{o_{1v}a_{n-1}} & J^{o_{1v}a_n} \\
J^{a_1\Delta} & J^{a_1o_{0h}} & J^{a_1o_{0v}} & J^{a_1o_{1h}} & J^{a_1o_{1v}} & \sigma^2_{\epsilon_{a_1}} & 0 & & 0 & 0 \\
J^{a_2\Delta} & J^{a_2o_{0h}} & J^{a_2o_{0v}} & J^{a_2o_{1h}} & J^{a_2o_{1v}} & 0 & \sigma^2_{\epsilon_{a_2}} & & 0 & 0 \\
 & & \vdots & & & & & \ddots & & \\
J^{a_{n-1}\Delta} & J^{a_{n-1}o_{0h}} & J^{a_{n-1}o_{0v}} & J^{a_{n-1}o_{1h}} & J^{a_{n-1}o_{1v}} & 0 & 0 & & \sigma^2_{\epsilon_{a_{n-1}}} & 0 \\
J^{a_n\Delta} & J^{a_no_{0h}} & J^{a_no_{0v}} & J^{a_no_{1h}} & J^{a_no_{1v}} & 0 & 0 & & 0 & \sigma^2_{\epsilon_{a_n}}
\end{bmatrix} \quad (34)$$

The primary one studied in the following sections is the first diagonal element $\sigma^2_{\epsilon_\Delta}$. This is the lower bound on the estimate of the pixel separation Δ.

3 Effect of Atmospheric Turbulence on Bounds Calculations

Using the expanded FI matrices, the average lower bound on the estimate of the pixel separation and other parameters are calculated. In order to compute an analytical solution some additional parameters are required. The following parameters are used for generation of most of the graphs in this analysis.

- Aperture size of 1 meter
- Fried parameter (r_o) of 1 meter
- Focal length of 10 meters
- Object intensity of 0.1mW
- Grid size of 32 by 32 pixels
- Wavelength of 800nm

3.1 Normal Imaging System

This section discusses the average lower bound on the estimate of the pixel separation for a normal (i.e. non-polarimetric) sensor. The number of Zernike coefficients is varied and the impact on the average lower bound is shown if Fig. 1.

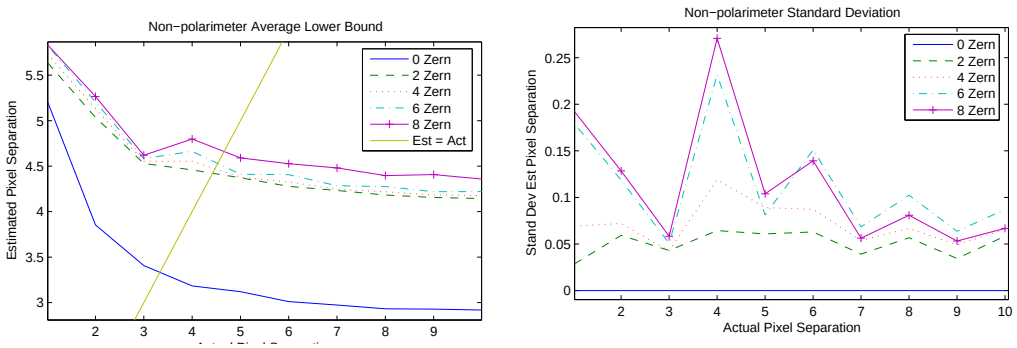

(a) Non-polarimeter Average Bounds

(b) Standard Deviation of Average Bounds

Figure 1: Average bound relative to pixel separation

The primary focus of this research is on the CRLB of the estimated pixel separation of the two point sources. Fig. 1(a) shows the average CRLB as the actual pixel separation in the model is changed. The lowest line is the basic model without any Zernike coefficients estimated. The upper grouping of lines are for estimates when two, four, six, and eight coefficients are added to the model. Fig. 1(b) shows the standard deviations of the data used to generate the bound plots to the left. The standard deviation for the model without any Zernike coefficients is on the bottom of the plot at values in the 10^{-14} range. Thus, introducing atmospheric turbulence into the model increases the lower bound. The bound follows a similarly shaped curve as the non-turbulent model. All plots amptotically approach some value as the separation gets larger. The determination of that value is discussed in Section 3.3.2.

3.2 Polarimeter Imaging System

Now that the behavior for the normal imaging system is known, the behavior of the polarimeter model is determined. Keeping the same parameter settings as the normal system, the polarimeter lower bound on the estimation of Δ is plotted against the actual pixel separation with the addition of various induced polarization states of the point sources.

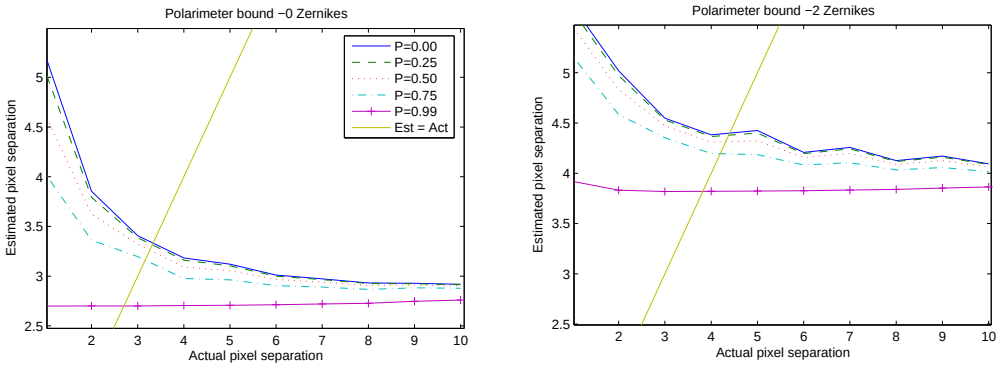

(a) Polarimeter without Zernike Coefficients

(b) Polarimeter with Zernikes 2 and 3

Figure 2: Average polarimeter bounds relative to pixel separation

Fig. 2(a) shows the effect of polarization on the average lower bound on the estimated pixel separation as the degree of polarization goes from zero to close to one. A note on the model regarding a completely polarized source is necessary here. With a degree of polarization of one, a discontinuity is reached and `Matlab`® produces NaNs for the plot. Therefore, a degree of polarization of 0.99 is chosen to show the average bound close to $p = 1$. One should also note that as the degree of polarization increases, the bound flattens out until the limit on the bound is reached for estimating the location of a single point source.

In Fig. 2(b), the estimates of the first two Zernike coefficients (piston is ignored) related to tilt are introduced. The bounds have a relative shift upward. The top line in the plot corresponds to the unpolarized source case and follows the grouping of lines seen in Fig. 1(a) for the normal imaging system. As the degree of polarization increases, the average lower bound decreases. The limit is approached as the degree of polarization approaches one. Based on a definition of minimum resolving power for the system located at the point where its estimate equals the actual, one can see that polarization effects can improve resolving power. For this particular set of parameters, the improvement is approximately 20 percent which is typical for most runs.

3.3 Other System Parameters

The effects of other parameters on the spatial frequency lower bound and other estimates are explored in this section. First, the effect the number of Zernike coefficients estimated have on the spatial frequency bound and on source intensity estimates are explored. Next, all parameters are fixed and just the source intensities are varied to explore its effect on the bound. Finally, a very brief look is taken at the effect of the Fried parameter on the model. It is fixed at eight times smaller than the aperture and the impact of partial compensation by an adaptive optics (AO) system is explored.

3.3.1 Effect of Number of Zernike Coefficients Estimated

An understanding of how the model changes as the number of Zernike coefficients estimated increases is explored. It is noted that the average lower bound on the estimate of Δ increases as the number of coefficients increases. In order to quantify the change, all the parameters are fixed. The average pixel separation estimate is then calculated at an actual pixel separation of five pixels. Two hundred iterations were averaged for both the normal imaging system and the polarimeter at each polarization setting for every additional Zernike coefficient up to 85.

Fig. 3(a) shows the result for the normal imaging system. Fig. 3(b) shows the results for the polarimeter for each of the polarization settings. As the degree of polarization increases the plot lines decrease but retain similar shapes. The plot for the polarization line close to one gets more erratic as the degree of polarization gets closer to one. This is due to the discontinuity in the model when the degree of polarization is one. All of the lines are similar in shape to the plot in Fig. 3(c). This is the cumulative sum of the expected values for the covariance of the Zernike coefficients.

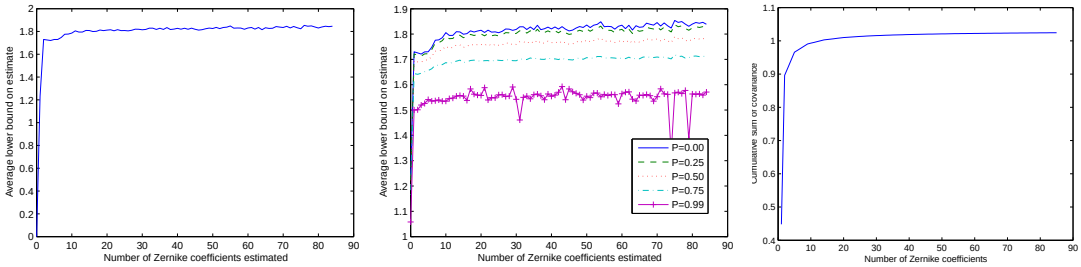

(a) Normal average pixel separation bound (b) Polarimeter average pixel separation bound (c) Zernike coefficient covariance cumulative sum

Figure 3: Average bound relative to number of Zernike coefficients estimated

Although the average spatial frequency CRLB changes as the number of Zernike coefficients changes, the average CRLB of the point source intensity estimates change very little. Very slight variations of the bounds are noted in Fig. 4. When the model is unpolarized all estimates for the point sources have the same values. As the degree of polarization increases, the intensities of O_{oh} and O_{1v} increase in the model with a corresponding increase in the average lower bound of their estimates. The converse is true for O_{ov} and O_{1h}.

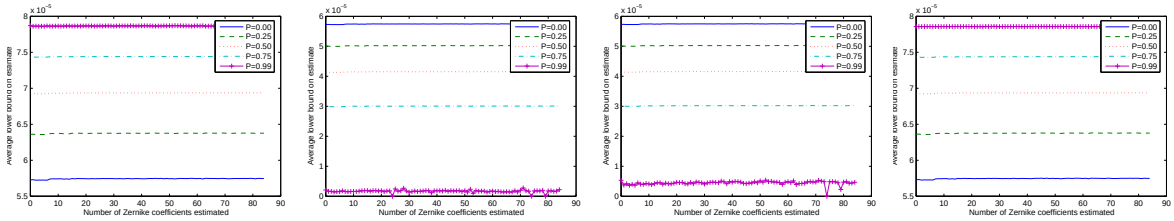

(a) Estimates of Ooh (b) Estimates of Oov (c) Estimates of O1h (d) Estimates of O1v

Figure 4: Average point source intensity estimates relative to number of zernike coefficients estimated

3.3.2 Effect of Light Intensity on Bounds

Another parameter that affects the model's estimates is the light intensity of the point sources. For simplicity both source are fixed at the same magnitude. While all other parameters are fixed, the intensity is adjusted to produce the curve shown in Fig. 5. As the intensity is increased, the average spatial frequency CRLB decreases asymptotically to one pixel width. Conversely, as the intensity is decreased, the average spatial frequency CRLB increases.

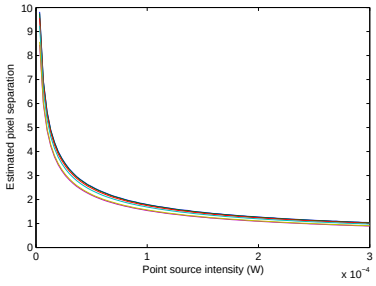

Figure 5: Average bound relative to point source intensity

3.3.3 Effects of Fried parameter and Adaptive Optics

The rest of this paper assumes a D/r_o fraction of one. Where r_o is the Fried parameter (r_o)[1]. This section, however, discusses the effect of an r_o value less than the aperture size such that $D/r_o = 1/8$. The plots shown in Fig. 6 reflect this increased 'turbulence'. The left image, Fig. 6(a), plots the average spatial frequency lower bound for each polarization case. The results are from the averaging of 200 independent iterations at each polarization setting.

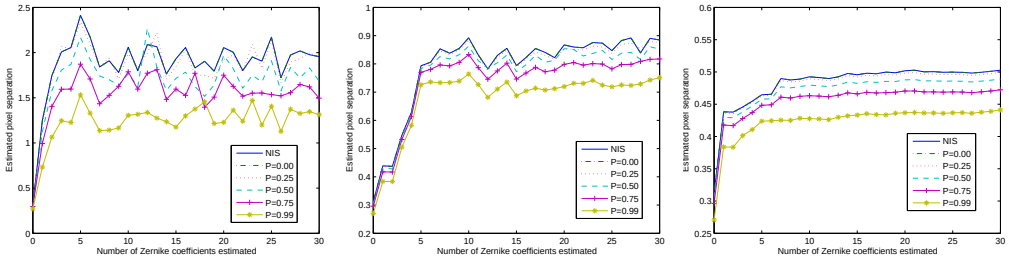

(a) No AO (b) 95 percent tilt removed (c) AO system

Figure 6: Average point source intensity estimates relative to number of zernike coefficients estimated

The impact of an AO system is also modeled. Assuming an AO system can remove 95 percent of the tilt coefficients, the results shown in Fig. 6(b) are attained. The initial part of the plots is greatly smoothed out and the overall bounds are improved significantly. For the last case, the following characteristics are assumed regarding the 'AO' system's compensation of abberations:

- 95 percent tip/tilt compensated
- 80 percent defocus and astigmatism compensated
- 50 percent coma, trifoil, and spherical compensated

The bounds are significantly smoothed out, in Fig. 6(c), for the entire range of Zernike coefficients. The results show that the model can incorporate AO parameters for estimation of the spatial frequency CRLB under different atmospheric conditions. Thus, if one knows the performance characteristics of an AO system and the r_o value during the observation, one can use the model to predict the lower bound on spatial frequency resolution that can be attained by any algorithm.

4 Conclusions

This research explores the CRLB of a polarimeter with comparison to a non-polarimetric imaging system. Several parameters in the model affect the spatial frequency CRLB. Of these, the number of Zernike coefficients estimated, the intensity of the sources, and the degree of polarization all having varying degrees of effect on the bound. The non-polarimetric imaging system and the unpolarized curve for the polarimeter are very similar. As the degree of polarization increases, the polarimeter's resolving power increases. Thus, given polarization effects in images, the results of this analysis show that a polarimeter has the potential for increased resolving power over traditional imaging systems.

References

[1] Roggemann M. C. and Welsh B. M. *Imaging Through Turbulence*. CRC Press, 1996.

[2] Strong D. and Cain S. "Spatial Frequency Bounds of a Polarimetric Sensor." *Proceedings of the 2005 AMOS Conference*. September 2005.

[3] VanTrees H. L. *Detection, Estimation, and Modulation Theory: Part I*. A Wiley Interscience Publication, 605 Third Avenue, New York, NY 10158-0012: John Wiley & Sons, Inc., 2001.